Research Article

A Magnetically Recoverable $V_2O_5/SiO_2/Fe_3O_4$ Catalyst for the Sustainable Valorization of Glycerol to Solketal

Ado Ibrahim Yargaya, Vannapa Luckanawat and Kittichai Chaiseeda*
Organic Synthesis, Electrochemistry and Natural Product Research Unit (OSEN), Department of Chemistry, Faculty of Science, King Mongkut's University of Technology Thonburi, Bangkok, Thailand

Piyarat Trikittiwong
Department of Industrial Chemistry, Faculty of Applied Science, King Mongkut's University of Technology North Bangkok, Bangkok, Thailand
Integrated Chemistry Research Center for Sustainable Technology, King Mongkut's University of Technology North Bangkok, Bangkok, Thailand

Manuela Stan
National Institute for Research and Development of Isotopic and Molecular Technologies, Cluj-Napoca, Romania

* Corresponding author. E-mail: kittichai.cha@kmutt.ac.th DOI: 10.14416/j.asep.2026.05.005
Received: 18 December 2025; Revised: 1 February 2026; Accepted: 12 March 2026; Published online: 12 May 2026

Abstract
The sustainable valorization of surplus glycerol produced from biodiesel manufacturing is a critical challenge and opportunity in environmental and green chemical engineering. In this study, a magnetically recoverable $V_2O_5/SiO_2/Fe_3O_4$ catalyst was synthesized via thermal decomposition and applied to the ketalization of glycerol with acetone for the production of solketal, a high-value fuel additive and green solvent. Comprehensive structural and surface characterization using XRD, BET, SEM, HR-TEM, VSM, XRF, FTIR, and XPS confirmed the successful integration of all components, high surface accessibility, mesoporosity, strong magnetic response, and the coexistence of V^{5+}/V^{4+} redox species. Under optimized reaction conditions, the 20 wt% $V_2O_5/SiO_2/Fe_3O_4$ catalyst achieved a glycerol conversion of 91.34% with a solketal selectivity of 99.65% after 4 h at reflux. The catalyst exhibited excellent stability and reusability, maintaining high catalytic performance over successive cycles with only a slight decrease in activity, attributed to partial catalyst loss during recovery. This work demonstrates an effective route for the environmentally sustainable conversion of biodiesel-derived glycerol into value-added chemicals using a low-cost, easily recoverable catalyst platform with strong potential for practical implementation.

Keywords: Biodiesel by-product utilization, Glycerol valorization, Heterogeneous catalysis, Magnetic catalyst, Solketal synthesis, Sustainable chemical engineering

1 Introduction

The global transition toward sustainable energy systems has significantly increased the production and consumption of biodiesel as an alternative to conventional fossil fuels. However, biodiesel manufacturing generates substantial amounts of glycerol as a byproduct, accounting for approximately 10 wt% of the total biodiesel output. Although glycerol is non–toxic and biodegradable, its oversupply and limited direct utilization have markedly reduced its market value, thereby affecting the overall economic viability of biodiesel production [1]–[4]. Consequently, the sustainable valorization of surplus glycerol into value–added chemicals has become an important research focus in environmental and green chemical engineering.

Extensive efforts have been devoted to converting glycerol into high–value products through various catalytic pathways, encompassing hydrogenolysis, oxidation, esterification, and ketalization, as summarized in Table S1 (Supporting Information).

Among these pathways, the condensation of glycerol with carbonyl compounds has received particular attention because it yields solketal, a useful fuel additive that significantly improves the physicochemical properties of biodiesel and gasoline blends. The direct utilization of glycerol remains limited due to its low calorific value, high viscosity, poor miscibility with hydrocarbon fuels, and thermal instability [5], [6]. When glycerol reacts with acetone, solketal ((2,2–dimethyl–1,3–dioxolan–4–yl)methanol) and a minor six–membered acetal, 2,2–dimethyl–1,3–dioxan–5–ol, are formed via an acid–catalyzed ketalization (acetalization) reaction, producing water as a byproduct (Figure 1) [7].

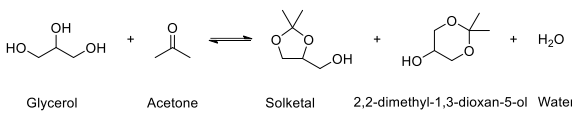

Figure 1: Ketalization of glycerol with acetone.

The beneficial fuel properties of solketal have been clearly demonstrated in previous investigations. Mota et al. reported that solketal enhances the octane number of gasoline, suppresses gum formation, and improves fuel stability, making it an attractive renewable oxygenated additive [8]. As a biodiesel additive, solketal improves cold flow behavior and oxidation resistance [9], [10]. In addition, solketal has gained attention as a green solvent and chemical intermediate for applications in cleaning formulations, pharmaceutical manufacturing, refrigeration systems, resin synthesis, and coating technologies, further expanding its commercial relevance [4], [5], [11].

Despite its advantages, glycerol ketalization faces thermodynamic and operational challenges, including a low equilibrium constant and the continuous generation of water, which shifts the reaction backward. Moreover, partial immiscibility between glycerol and acetone limits mass transfer and reduces reaction efficiency, often necessitating the use of excess acetone to drive the reaction toward product formation [12]. Both Brønsted and Lewis acid sites are essential for catalyzing the reaction, and early studies frequently employed homogeneous acids such as sulfuric acid, hydrochloric acid, and *p*–toluenesulfonic acid. However, corrosion issues, product contamination, catalyst recovery difficulty, and wastewater generation significantly restrict their sustainable application [3], [13]. These drawbacks have motivated the development of heterogeneous catalytic systems that offer improved environmental compatibility, ease of separation, and reusability.

Although solid acid catalysts provide significant operational advantages over homogeneous acids, their performance is often compromised by water adsorption on hydrophilic surfaces, which blocks active sites and competitively inhibits the reaction. As a result, catalysts with high water tolerance, structural stability, and balanced acidity are highly desirable for practical glycerol valorization [14]. In response to these challenges, a wide range of heterogeneous catalysts have been investigated, including carbon–based materials [15], [16], silica-based catalysts [17–20], polymer–supported acids [14], sulfonic acid–functionalized silica catalysts [21], and metal–organic frameworks (MOFs) [22]. Each class offers distinct benefits in terms of surface chemistry, acidity control, and stability.

Several catalytic systems have demonstrated promising performance for solketal synthesis. Rajkumari *et al.,* developed sulfonic acid–functionalized Fe_3O_4 nanoparticles that achieved high activity and recyclability [23]. Singh *et al.,* reported high conversion and selectivity using HPMo/AlTUD–1 catalysts [24]. Ao *et al.,* introduced biochar–derived carbon nanodots as sustainable catalysts with significant solketal yields [15]. Acid–modified pyrolytic carbon materials from waste tires have also shown effective catalytic performance [25]. Additionally, Wang *et al.,* developed UiO–SO_3H–30 catalysts with excellent glycerol conversion and solketal selectivity [26]. These studies clearly indicate that catalyst composition and surface functionality strongly influence ketalization efficiency.

Among various catalyst supports, Fe_3O_4 (magnetite) has emerged as a highly attractive material due to its intrinsic magnetic properties, moderate surface area, and chemical stability [27]. The incorporation of Fe_3O_4 enables rapid catalyst recovery through external magnetic separation, significantly reducing post–reaction processing steps and improving long–term economic viability. Recent studies on Fe_3O_4–based composite materials have demonstrated that magnetic supports not only facilitate efficient separation and reusability but also maintain structural and magnetic stability over multiple operational cycles, highlighting their

suitability for sustainable catalytic applications [28]–[30]. In addition, Fe_3O_4 has been shown to promote improved dispersion of active species when integrated into composite architectures, which can contribute to enhanced catalytic performance and durability.

In glycerol ketalization, the design of an effective heterogeneous catalyst must simultaneously address acidity control, stability under water–forming equilibrium conditions, and catalyst recoverability. Many solid acid catalysts reported to date, particularly sulfonated materials and strongly Brønsted–acidic systems, exhibit high initial activity but often suffer from side reactions, water–induced deactivation, acid leaching, and limited recyclability [16], [21]. To overcome these limitations, we hypothesize that integrating V_2O_5, SiO_2, and Fe_3O_4 into a single catalyst architecture can synergistically address the key shortcomings of existing glycerol ketalization catalysts by balancing acidity, dispersion and stability, and magnetic recoverability. In this multifunctional structure, V_2O_5 provides predominantly Lewis acidic sites that activate the carbonyl group of acetone and promote selective ketalization [31], [32], SiO_2 offers a high–surface–area and chemically robust platform for uniform dispersion, enhanced accessibility of active sites, and improved tolerance toward water generated during the reaction [18], [20], [33], [34], and Fe_3O_4 supplies magnetic functionality for facile post–reaction separation and catalyst reuse [27], [35]. While binary V_2O_5/Fe_3O_4 systems have been previously reported mainly as proof–of–concept magnetic catalysts [36], they do not address dispersion control or stability under water–forming reaction conditions. The present $V_2O_5/SiO_2/Fe_3O_4$ catalyst, therefore, represents a rational and sustainable strategy for converting biodiesel–derived glycerol into solketal with improved activity, stability, and operational durability.

2 Materials and Methods

2.1 *Materials*

Iron(III) chloride hexahydrate ($FeCl_3 \cdot 6H_2O$, Tian-Nam Chemical Industrial Trade), iron(II) chloride tetrahydrate ($FeCl_2 \cdot 4H_2O$, 98%, Loba Chemie), tetraethyl orthosilicate (TEOS, $C_8H_{20}O_4Si$, >98.0%, TCI), ammonia solution (NH_4OH, 25%, Thomas Baker, India), and ammonium metavanadate (NH_4VO_3, 99.0%, KemAus) were used for the synthesis of Fe_3O_4, SiO_2/Fe_3O_4, and $V_2O_5/SiO_2/Fe_3O_4$ catalysts. Vanadium pentoxide (V_2O_5, 99.0%, Thomas Baker, India) and silicon dioxide (SiO_2, 99.0%, Thomas Baker, India) were employed as reference standards for both physicochemical characterization and comparative catalytic testing in glycerol ketalization. Acetone (C_3H_6O, Merck KGaA, Darmstadt, Germany) was used as both solvent and reactant, while hydrochloric acid (HCl, 37%, RCI) was used for pH adjustment. Glycerol ($C_3H_8O_3$, 99.5%, Carlo Erba) and solketal ($C_6H_{12}O_3$, 97.0%, Acros) were used as standard compounds for product quantification. Toluene ($C_6H_5CH_3$, 99.5%, AR grade, Thomas Baker, India) was used as the internal standard in gas chromatography (GC) analysis.

2.2 *Synthesis of Fe_3O_4*

Fe_3O_4 nanoparticles were synthesized via a co–precipitation method. Iron(III) chloride hexahydrate ($FeCl_3 \cdot 6H_2O$, 16.25 g, 60.2 mmol) was dissolved in 100 mL of distilled water, and iron(II) chloride tetrahydrate ($FeCl_2 \cdot 4H_2O$, 6.35 g, 31.7 mmol) was separately dissolved in 100 mL of distilled water. The two solutions were mixed in a glass beaker and stirred continuously at 70 °C. Aqueous ammonia solution (NH_4OH) was then added dropwise until the pH of the mixture reached pH 10, resulting in the formation of a black precipitate. The precipitate was collected by filtration, washed repeatedly with deionized water to remove residual ions, and dried at 80 °C prior to further use [35].

2.3 *Synthesis of SiO_2/Fe_3O_4*

Fe_3O_4 nanoparticles (1.0 g, 4.31 mmol) were first treated with 25 mL of 0.5 M aqueous HCl under sonication for 10 min to activate the surface. The particles were magnetically separated and washed five times with deionized water until the pH of the supernatant reached approximately 4. The treated Fe_3O_4 was then dispersed in a mixed solvent consisting of ethanol (60 mL), deionized water (100 mL), and concentrated ammonia solution (10 mL, 25 wt%), resulting in a final pH of about 10, and the suspension was maintained under vigorous stirring at room temperature. Tetraethyl orthosilicate (TEOS, 0.693 g, 3.33 mmol) was added dropwise under continuous stirring, and the mixture was stirred for 3 h to allow TEOS hydrolysis and condensation, leading to the formation of a silica coating on the Fe_3O_4 nanoparticles. The resulting SiO_2/Fe_3O_4 composite was magnetically separated using an external magnet, washed repeatedly with ethanol and deionized water

to remove residual reactants, and dried overnight at 80 °C prior to use [34].

2.4 *Synthesis of V_2O_5/Fe_3O_4 and $V_2O_5/SiO_2/Fe_3O_4$*

Ammonium metavanadate (NH_4VO_3, 0.26 g, 2.22 mmol) was dissolved in 75 mL of deionized water in a 250 mL beaker and heated at 120 °C under continuous stirring until the solution color changed from white to yellow–orange, indicating the formation of vanadium species in solution. The as–prepared Fe_3O_4 or SiO_2/Fe_3O_4 support (1.0 g) was added to the vanadium precursor solution under continuous stirring, and the resulting suspension was maintained at 120 °C for 1 h to ensure complete solvent evaporation. The obtained solid was then ground into a fine powder and subsequently calcined in a muffle furnace at 300 °C for 3 h in air to obtain the final V_2O_5/Fe_3O_4 or $V_2O_5/SiO_2/Fe_3O_4$ catalyst [36].

2.5 *Catalytic ketalization of glycerol*

Glycerol (1 mmol, 92.09 mg), acetone (20 mL; density = 0.784 g mL^{-1}), and the catalyst (40 mg) were charged into a 50 mL two–neck round–bottom flask equipped with an overhead mechanical stirrer. The mixture was stirred at 350 rpm for 10 min to ensure homogeneity and then heated to the reflux temperature of acetone (56 °C) under continuous stirring. The reaction was allowed to proceed for 4 h under reflux conditions.

After completion, the reaction mixture was cooled to room temperature, and 35 mg of toluene was added as an internal standard. The catalyst was separated using an external magnetic bar, and the clear supernatant was withdrawn using a syringe and transferred to a GC vial.

Analysis was performed by gas chromatography (GC) using a Shimadzu GC–2030 system equipped with a flame ionization detector (FID) and a VF–WAXms capillary column (30.0 m length, 0.25 mm internal diameter, 0.25 µm film thickness). Glycerol conversion and solketal selectivity were quantified using the internal standard method, with toluene employed as the internal standard. The GC oven temperature program was as follows: an initial temperature of 60 °C (0 min hold), ramped at 20 °C min^{-1} to 250 °C, followed by a 1 min hold at 250 °C, giving a total run time of 10.5 min. Glycerol, solketal, and acetal were identified by comparison of their retention times with those of authentic reference standards analyzed under identical conditions.

2.6 *Calculation of conversion and selectivity*

$$\text{glycerol conversion (\%)} = \frac{\text{(initial glycerol (mmol) - remaining glycerol (mmol)}}{\text{initial glycerol (mmol)}} \times 100$$

$$\text{solketal selectivity (\%)} = \frac{\text{solketal yield (\%)}}{\text{glycerol conversion (\%)}} \times 100$$

2.7 *Recyclability test*

Catalyst reusability was evaluated to assess the operational stability and economic feasibility of the prepared catalyst. Recyclability experiments were conducted under the optimized reaction conditions described above.

After each reaction cycle, the catalyst was separated from the reaction mixture by magnetic decantation using an external magnet and washed with acetone (10 mL per wash) under stirring at 350 rpm for 5 min. This washing procedure was repeated twice to remove adsorbed reactants and products.

The recovered catalyst was then dried at 100 °C for 5 h, weighed to estimate catalyst loss, and reused directly in the subsequent cycle. Catalytic performance in each cycle was evaluated using the recovered catalyst mass without additional mass normalization, as the same catalyst sample was employed throughout the recyclability tests.

3 Results and Discussion

3.1 *Catalyst characterization*

The materials used in this study included both commercial and synthesized samples. Commercial vanadium pentoxide (V_2O_5) and silica (SiO_2), together with synthesized Fe_3O_4, SiO_2/Fe_3O_4, V_2O_5/Fe_3O_4, and $V_2O_5/SiO_2/Fe_3O_4$ catalysts, were characterized using a range of analytical techniques, including X–ray diffraction (XRD), X–ray fluorescence (XRF), nitrogen adsorption–desorption analysis (Brunauer–Emmett–Teller, BET), high–resolution transmission electron microscopy (HR–TEM), scanning electron microscopy (SEM), Fourier–transform infrared spectroscopy (FTIR), vibrating sample magnetometry (VSM), and X–ray photoelectron spectroscopy (XPS).

Crystallographic properties were analyzed by powder X–ray diffraction using a Bruker D8 θ–θ diffractometer equipped with a Cu Kα radiation source (λ = 1.5406 Å) and operated at 40 kV and 40 mA. Diffraction patterns were recorded in the 2θ range of 10–100° with a step size of 0.02° and a counting time of 0.4 s per step. An Eiger2R 250K hybrid pixel

detector was used, with fixed divergence and Soller slits and without an incident–beam monochromator.

Elemental composition and metal loading were determined by X–ray fluorescence spectroscopy (XRF, Fischerscope X–ray XUV 773). Textural properties, including specific surface area, pore volume, and pore size distribution, were obtained from nitrogen adsorption–desorption isotherms using a surface area analyzer (Quantachrome Autosorb–iQ3–MP/Kr).

Surface morphology, microstructure, and elemental distribution were examined by high–resolution transmission electron microscopy coupled with energy–dispersive X–ray spectroscopy (HR–TEM/EDS, JEOL JEM–ARM200F) and field–emission scanning electron microscopy (FE–SEM, JEOL JSM–IT800). Fourier–transform infrared (FTIR) spectra were collected using an ATR accessory (Thermo Scientific Nicolet iS50). Spectra were recorded over the wavenumber range of 400–4000 cm^{-1} with an acquisition time of 32 s.

Magnetic properties were measured using a vibrating sample magnetometer (VSM, Lake Shore Cryotronics 8600 Series) under an applied magnetic field of up to 20 kOe with a field step size of 10 Oe. The maximum magnetic field strength during measurement was 2.76 T. The oxidation states and surface chemical composition of the samples were analyzed by X–ray photoelectron spectroscopy (XPS, JEOL JPS–9010MC).

3.1.1 XRD analysis

X–ray diffraction (XRD) was employed to identify the crystalline phases and evaluate the crystallinity of the prepared materials, thereby confirming the successful formation of the designed composite catalysts (Figure 2).

The XRD pattern of commercial V_2O_5 (black) exhibits sharp diffraction peaks at 2θ = 15.34°, 20.25°, 21.70°, 26.13°, 31.00°, 32.37°, and 34.33°, which are indexed to the (200), (001), (101), (110), (301), (011), and (310) crystallographic planes, respectively, corresponding to orthorhombic V_2O_5 (ICDD PDF No. 04–007–0398). The sharp and well–defined reflections indicate the high crystallinity of the vanadium oxide phase.

The XRD pattern of synthesized Fe_3O_4 (red) shows characteristic reflections at 2θ = 30.30°, 35.61°, 57.23°, and 62.89°, assigned to the (220), (311), (511), and (440) planes of the cubic spinel structure of magnetite (ICDD PDF No. 01–088-0866). A weak additional peak at 32.57°, marked with an asterisk (★), is attributed to a trace impurity phase. Due to its very low intensity, no crystallographic plane was assigned, indicating only a minor deviation from phase–pure magnetite.

The XRD pattern of commercial SiO_2 (blue) displays a broad diffraction band centered at 2θ = 23.08°, characteristic of amorphous silica (ICDD PDF No. 04–025–3100), confirming its non–crystalline nature.

For the SiO_2/Fe_3O_4 composite, the characteristic reflections of Fe_3O_4 at 2θ = 30.26°, 35.63°, 57.44°, and 62.91°–corresponding to the (220), (311), (511), and (440) planes–remain clearly visible, indicating preservation of the magnetite core structure after silica coating. No distinct crystalline SiO_2 reflections are observed, confirming that the silica phase remains predominantly amorphous. A weak reflection at 2θ = 53.74°, highlighted in orange, is assigned to the (422) plane of maghemite (γ–Fe_2O_3), suggesting slight surface oxidation of Fe_3O_4 during synthesis or handling.

The XRD pattern of the V_2O_5/Fe_3O_4 composite reveals the coexistence of orthorhombic V_2O_5 (black), magnetite Fe_3O_4 (red), and hematite α–Fe_2O_3 (pink). Diffraction peaks at 2θ = 24.14°, 33.13°, 40.89°, 49.47°, 54.08°, and 62.50° are indexed to the (–112), (–314), (–113), (–404), (–516), and (–114) planes of hematite, respectively (ICDD PDF No. 00–071–0073), indicating partial oxidation of magnetite during synthesis. Nevertheless, characteristic Fe_3O_4 reflections at 2θ = 35.63° and 57.59°, corresponding to the (311) and (511) planes, remain evident. In addition, a distinct peak at 2θ = 64.10°, assigned to the (512) plane of orthorhombic V_2O_5, confirms the successful incorporation of vanadium oxide into the composite.

The XRD pattern of the fresh ternary $V_2O_5/SiO_2/Fe_3O_4$ catalyst is dominated by Fe_3O_4 reflections at 2θ = 30.23°, 35.65°, and 57.39°, corresponding to the (220), (311), and (511) planes, confirming that magnetite retains its inverse spinel structure after composite formation. A minor reflection at 2θ = 63.05°, highlighted in orange, is assigned to the (440) plane of γ–Fe_2O_3 (ICDD PDF No. 04–021–3968), indicating limited surface oxidation. A faint high–angle peak at 2θ = 93.45°, indexed to the (722) plane of V_2O_5, suggests that vanadium oxide is highly dispersed and present in a low–crystallinity form.

For the spent catalyst, characteristic Fe_3O_4 reflections at 2θ = 30.27° and 35.58°, corresponding

to the (220) and (311) planes, respectively, are retained, demonstrating that the magnetite framework remains largely preserved after catalytic operation. An additional reflection at 2θ = 62.97°, corresponding to the (440) plane of γ–Fe_2O_3, indicates partial surface oxidation during the reaction. Despite this transformation, Fe_3O_4 remains the dominant crystalline phase, confirming the high structural stability of the catalyst under the applied reaction conditions.

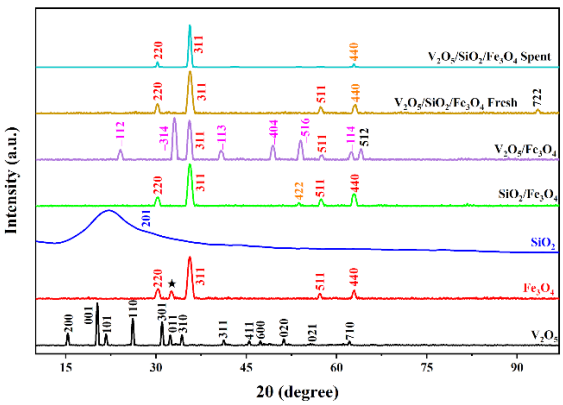

Figure 2: X–ray diffraction (XRD) patterns of commercial V_2O_5 and SiO_2, and the synthesized Fe_3O_4, SiO_2/Fe_3O_4, V_2O_5/Fe_3O_4, $V_2O_5/SiO_2/Fe_3O_4$ catalysts, and the spent $V_2O_5/SiO_2/Fe_3O_4$ catalyst.

3.1.2 XRF analysis

X–ray fluorescence (XRF) spectroscopy was employed to determine the elemental composition and oxide loading of the prepared composite catalysts, thereby verifying that the V_2O_5 content was consistent with the intended catalyst formulation. The results show that the V_2O_5/Fe_3O_4 sample contains 7.70 wt% V_2O_5 and 91.70 wt% Fe_3O_4, while the SiO_2/Fe_3O_4 catalyst consists of 7.36 wt% SiO_2 and 91.59 wt% Fe_3O_4. For the ternary $V_2O_5/SiO_2/Fe_3O_4$ system, the measured composition corresponds to 14.92 wt% V_2O_5, 7.50 wt% SiO_2, and 77.94 wt% Fe_3O_4. These values verify that the intended oxide components were successfully incorporated into the catalyst framework with controlled loading.

3.1.3 BET analysis

N_2 adsorption–desorption analysis was conducted to evaluate the surface area and pore structure of the prepared materials, which directly govern reactant accessibility to the active sites during glycerol ketalization, and the results are summarized in Table 1. Commercial SiO_2 exhibits the highest specific surface area (149.8 m^2 g^{-1}) and pore volume (1.30 cm^3 g^{-1}), consistent with its highly porous mesoporous structure, with an average pore diameter of 15.7 nm. In contrast, Fe_3O_4 nanoparticles display a lower surface area (75.6 m^2 g^{-1}) and pore volume (0.178 cm^3 g^{-1}), with a smaller pore diameter of 8.81 nm, reflecting a denser morphology with limited intrinsic porosity. Commercial V_2O_5 exhibits the lowest surface area (8.57 m^2 g^{-1}) and pore volume (0.025 cm^3 g^{-1}), confirming its compact, nonporous nature.

Table 1: Specific surface area, pore volume, and pore diameter of V_2O_5, Fe_3O_4, SiO_2, and composite catalysts determined by the BET method.

Samples	Surface Area (m^2 g^{-1})	Pore Volume (cm^3 g^{-1})	Pore Diameter (nm)
SiO_2	149.842	1.2980	15.733
Fe_3O_4	75.611	0.1779	8.810
V_2O_5	8.568	0.02499	3.618
V_2O_5/Fe_3O_4	25.203	0.2242	3.627
SiO_2/Fe_3O_4	82.012	0.4104	8.861
$V_2O_5/SiO_2/Fe_3O_4$	52.751	0.2635	3.630

The V_2O_5/Fe_3O_4 composite shows a notable improvement in surface area (25.2 m^2 g^{-1}) and pore volume (0.224 cm^3 g^{-1}) relative to pristine V_2O_5, demonstrating that Fe_3O_4 serves as an effective support that enhances dispersion of vanadium species and partially restores porosity. The SiO_2/Fe_3O_4 composite exhibits intermediate textural properties, with a specific surface area of 82.0 m^2 g^{-1} and pore volume of 0.410 cm^3 g^{-1}, indicating that the silica coating effectively increases surface area and pore volume while preserving a mesoporous structure (average pore diameter of 8.86 nm).

Notably, the ternary $V_2O_5/SiO_2/Fe_3O_4$ catalyst displays a surface area of 52.8 m^2 g^{-1}, pore volume of 0.264 cm^3 g^{-1}, and an average pore diameter of 3.63 nm. The reduction in pore size relative to SiO_2/Fe_3O_4 suggests that V_2O_5 species occupy the mesopores of the silica network, forming a denser structure while maintaining a sufficiently high surface area for catalytic applications [32].

The N_2 adsorption–desorption isotherms of the $V_2O_5/SiO_2/Fe_3O_4$ composite catalyst exhibit pronounced hysteresis loops characteristic of Type IV behavior, confirming the presence of mesoporosity and capillary condensation effects (Figure 3) [37]. These results demonstrate that the incorporation of SiO_2 and Fe_3O_4 substantially improves the textural properties of V_2O_5 by increasing surface area and

generating accessible pore networks. The synergistic combination of high–surface–area SiO_2 and magnetically recoverable Fe_3O_4 yields catalysts with well–developed porosity and enhanced accessibility of active sites, which is beneficial for heterogeneous catalytic applications.

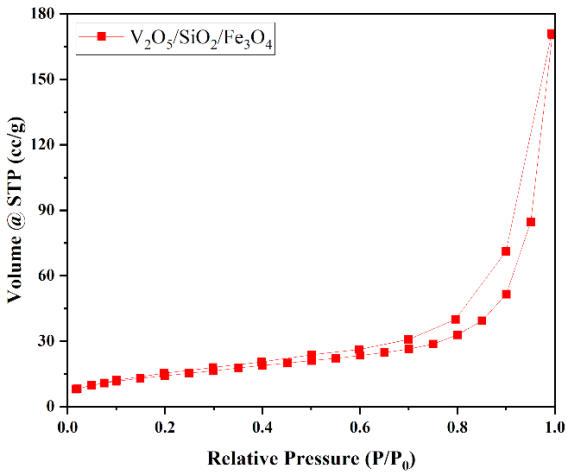

Figure 3: N_2 adsorption–desorption isotherms of the $V_2O_5/SiO_2/Fe_3O_4$ catalyst.

3.1.4 HR–TEM analysis

High–resolution transmission electron microscopy (HR–TEM) was employed to examine the nanoscale morphology and dispersion of the active species within the catalyst. The HR–TEM images of the $V_2O_5/SiO_2/Fe_3O_4$ catalyst reveal predominantly irregular and non–periodic contrast, indicating that most of the material—particularly the V_2O_5 phase—exists in an amorphous or highly dispersed state on the support (Figure 4). No distinct lattice fringes attributable to crystalline V_2O_5 are observed, confirming its low crystallinity, which is consistent with the weak vanadium–related reflections observed in the XRD patterns.

In contrast, well–defined lattice fringes with an interplanar spacing of 0.24 nm are clearly visible in the high–resolution image, which corresponds to the (311) crystalline plane of Fe_3O_4. This observation indicates that Fe_3O_4 retains a well–ordered crystalline structure within the composite.

The coexistence of amorphous vanadium oxide species and crystalline Fe_3O_4 confirms that V_2O_5 is finely dispersed across the SiO_2/Fe_3O_4 surface. Such high dispersion of active vanadium species is advantageous for catalytic reactions, as it increases the accessibility of reactive sites and promotes effective interaction between reactants and the catalyst surface.

3.1.5 TEM–EDS elemental mapping

TEM–EDS elemental mapping was employed to confirm the homogeneous spatial distribution of vanadium (V), silicon (Si), iron (Fe), and oxygen (O) throughout the $V_2O_5/SiO_2/Fe_3O_4$ composite catalyst (Figure 5). The uniform dispersion of vanadium species across the SiO_2/Fe_3O_4 support indicates effective incorporation of V_2O_5 without significant aggregation, which is beneficial for maximizing accessible active sites.

Such homogeneous elemental distribution is essential for achieving high catalytic efficiency, as it maximizes the exposure of active sites and minimizes diffusion limitations caused by particle clustering. The excellent dispersion of vanadium oxide is consistent with the XRD results, which indicate that V_2O_5 is present in a highly dispersed or low–crystallinity state. These structural features contribute to improved catalytic stability and resistance to deactivation, supporting the suitability of the catalyst for repeated reaction cycles without significant loss of activity.

3.1.6 SEM analysis

Scanning electron microscopy (SEM) was employed to examine the surface morphology, particle aggregation, and dispersion behavior of the prepared materials, as these structural features strongly influence catalytic accessibility and performance.

SEM micrographs of the samples recorded at 50,000× magnification (Figure 6) reveal distinct morphological characteristics for each catalyst component and composite. Commercial V_2O_5 (Figure 6(a)) exhibits a well–defined rod–like morphology consisting of elongated crystalline structures with smooth surfaces. This characteristic morphology is consistent with the orthorhombic phase of V_2O_5 [31] and indicates a high degree of crystallinity, which is in agreement with the sharp diffraction peaks observed in the XRD results. However, such compact crystalline structures provide limited external surface area, consistent with the low BET surface area measured for V_2O_5.

Fe_3O_4 nanoparticles (Figure 6(b)) display a highly agglomerated granular morphology in which nanosized particles form dense clusters. This agglomeration is typical for magnetic materials and is attributed to strong dipole–dipole interactions among

Fe_3O_4 particles, which drive the formation of compact aggregates and reduce effective surface accessibility [33]. Although magnetite provides magnetic recoverability, excessive aggregation may impede catalytic efficiency when used alone as a support.

Amorphous SiO_2 (Figure 6(c)) shows a fluffy and sponge–like morphology composed of loosely packed nanoparticles, resulting in a highly porous structure. This morphology is consistent with its high BET surface area and large pore volume, confirming the suitability of SiO_2 as an effective support material for dispersing catalytically active phases.

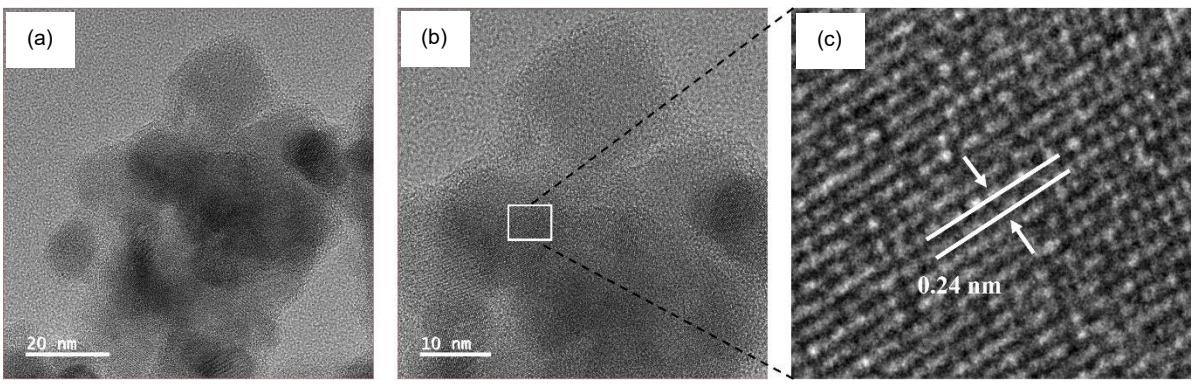

Figure 4: HR–TEM images of the $V_2O_5/SiO_2/Fe_3O_4$ composite catalyst: (a, b) representative micrographs showing particle morphology and dispersion, and (c) the corresponding lattice–fringe image indicating the interplanar spacing.

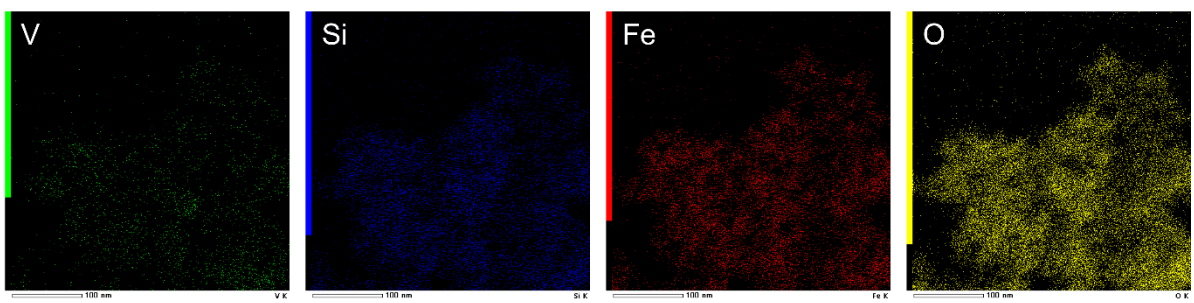

Figure 5: EDS elemental mapping images showing the spatial distribution of V, Si, Fe, and O within the $V_2O_5/SiO_2/Fe_3O_4$ catalyst.

In the SiO_2/Fe_3O_4 composite (Figure 6(d)), Fe_3O_4 particles are uniformly coated by a silica layer, forming a core–shell–like structure with a more structured and textured morphology. Compared with pristine Fe_3O_4, particle agglomeration is greatly reduced, indicating that the silica coating effectively suppresses magnetic clustering while preserving porosity. This coating layer enhances particle dispersion, improves surface stability, and maintains accessibility of active sites by preventing direct magnetic interactions between Fe_3O_4 cores.

The binary V_2O_5/Fe_3O_4 catalyst (Figure 6(e)) displays a highly agglomerated morphology in which the original rod–like structure of V_2O_5 is no longer distinguishable. Instead, dense composite clusters are formed, indicating poor dispersion of vanadium oxide on the Fe_3O_4 support and limited development of a porous network. This dense structure supports the XRD observation of partial oxidation to hematite and suggests that direct immobilization of V_2O_5 on Fe_3O_4 leads to unfavorable aggregation and reduced surface exposure.

In contrast, the ternary $V_2O_5/SiO_2/Fe_3O_4$ catalyst (Figure 6(f)) exhibits a porous, fluffy, and interconnected architecture in which oxide particles are uniformly distributed throughout the silica framework. The presence of SiO_2 effectively suppresses severe agglomeration and facilitates homogeneous dispersion of vanadium species on the support. This open morphology enhances surface

accessibility and provides efficient pathways for reactant diffusion, which are essential for catalytic reactions.

Overall, SEM analysis confirms that the incorporation of SiO_2 plays a critical role in controlling particle aggregation and improving the dispersion of V_2O_5 on the Fe_3O_4 support. The synergistic combination of porous SiO_2 and magnetic Fe_3O_4 produces a structurally optimized catalyst with enhanced accessibility of active sites, explaining the superior catalytic performance and stability observed for the $V_2O_5/SiO_2/Fe_3O_4$ system.

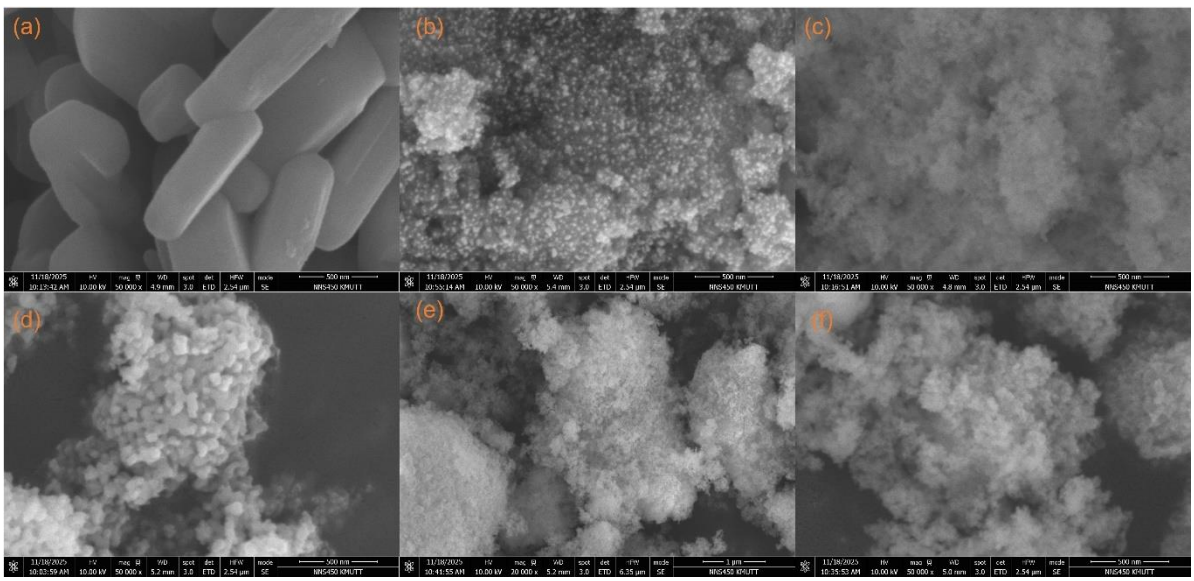

Figure 6: SEM images recorded at 50,000× magnification of (a) V_2O_5, (b) Fe_3O_4, (c) SiO_2, (d) SiO_2/Fe_3O_4, (e) V_2O_5/Fe_3O_4, and (f) $V_2O_5/SiO_2/Fe_3O_4$ catalysts.

3.1.7 FTIR analysis

Fourier transform infrared (FTIR) spectroscopy was employed to identify surface functional groups and probe metal–support interactions in the composite catalysts. FTIR spectra of V_2O_5, Fe_3O_4, SiO_2, SiO_2/Fe_3O_4, V_2O_5/Fe_3O_4, and $V_2O_5/SiO_2/Fe_3O_4$ are presented to elucidate bonding interactions and structural evolution within the catalyst system (Figure 7).

Pure V_2O_5 exhibits characteristic vibrational bands at 996 cm^{-1}, attributed to terminal V=O stretching, and at 803 cm^{-1} corresponding to bridging V–O–V vibrations. These features confirm the presence of the typical vanadium oxide framework. The Fe_3O_4 spectrum shows a broad absorption band centered at 3113 cm^{-1} associated with O–H stretching, along with an H–O–H bending vibration at approximately 1620 cm^{-1}, both arising from surface hydroxyl groups or adsorbed water. A weak band near 1400 cm^{-1} is assigned to carbonate–like surface species. Two prominent Fe–O lattice vibrational bands appear in the low–wavenumber region: one at approximately 530–560 cm^{-1} corresponding to Fe–O stretching at tetrahedral sites and another at 420–450 cm^{-1} assigned to octahedral Fe–O vibrations, confirming the inverse spinel structure of magnetite and consistent with reported literature [38].

The spectrum of SiO_2 displays the typical absorption bands associated with siloxane networks: a strong asymmetric Si–O–Si stretching vibration at 1083 cm^{-1}, a symmetric stretching band near 800 cm^{-1}, and a rocking vibration around 454 cm^{-1}. Upon coating SiO_2 onto Fe_3O_4 (SiO_2/Fe_3O_4), the asymmetric Si–O–Si band shifts to 1068 cm^{-1}, indicating interaction between the silica layer and the magnetic core. Concurrently, Fe–O stretching bands appear at 543 cm^{-1} and 431 cm^{-1}, assigned to tetrahedral and octahedral sites, respectively. The Si–O–Si bending vibration likely overlaps with Fe–O absorptions in this region.

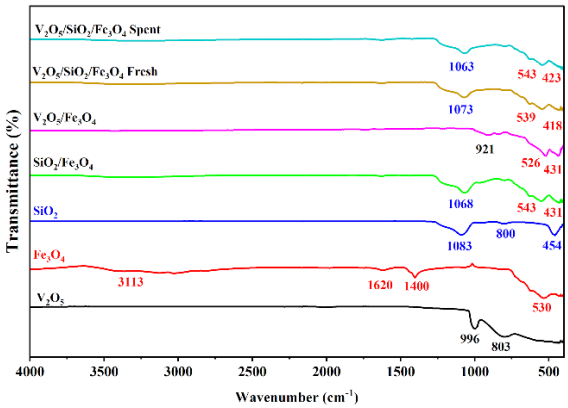

Figure 7: FTIR spectra of V_2O_5, Fe_3O_4, SiO_2, SiO_2/Fe_3O_4 and V_2O_5/Fe_3O_4, and the fresh and spent $V_2O_5/SiO_2/Fe_3O_4$ catalysts.

In the V_2O_5/Fe_3O_4 composite, a vanadium–oxygen band is observed at approximately 921 cm^{-1}, corresponding to a shifted V=O vibration caused by interaction with the iron oxide support. Characteristic Fe–O bands remain visible at 526 cm^{-1} and 431 cm^{-1}. For the ternary $V_2O_5/SiO_2/Fe_3O_4$ catalyst, the asymmetric Si–O–Si stretching mode is located at 1073 cm^{-1}, while Fe–O lattice vibrations appear at 539 cm^{-1} (tetrahedral) and 418 cm^{-1} (octahedral). Vanadium–oxygen vibrations are weak or shifted, reflecting strong interactions between vanadium species and the composite support and suggesting high dispersion of V_2O_5 within the silica–magnetite matrix.

After the fourth reaction cycle, only minor shifts in the FTIR bands were observed. The asymmetric Si–O–Si stretching vibration shifted slightly to 1063 cm^{-1}, while the Fe–O lattice vibrations appeared at 543 cm^{-1} and 423 cm^{-1}, corresponding to tetrahedral and octahedral sites, respectively. These subtle changes indicate that the catalyst framework remains largely intact, confirming the high structural stability of the $V_2O_5/SiO_2/Fe_3O_4$ catalyst after repeated reuse.

Overall, FTIR analysis confirms the successful integration of V_2O_5 and SiO_2 onto the Fe_3O_4 support and provides evidence of chemical interactions among the three components, which contribute to the structural stability and catalytic functionality of the composite system.

3.1.8 VSM analysis

Vibrating sample magnetometry (VSM) was employed to evaluate the magnetic properties of Fe_3O_4, SiO_2/Fe_3O_4, V_2O_5/Fe_3O_4, and $V_2O_5/SiO_2/Fe_3O_4$ catalysts, and the corresponding room–temperature hysteresis loops are presented in Figure 8. All samples exhibit narrow and symmetric hysteresis loops with rapid saturation under both positive and negative applied magnetic fields, confirming their suitability for efficient magnetic separation and recovery.

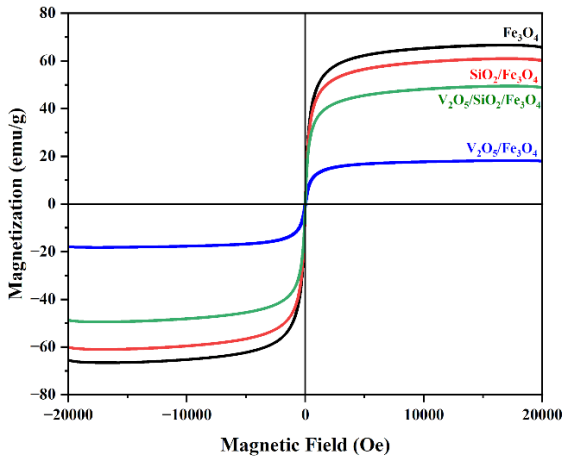

Figure 8: VSM hysteresis loops of Fe_3O_4 (black), SiO_2/Fe_3O_4 (red), V_2O_5/Fe_3O_4 (blue), and $V_2O_5/SiO_2/Fe_3O_4$ (green) catalysts.

The magnetic hysteresis parameters reveal very low coercivity (Hc) values of 5.38, 5.79, 14.00, and 6.23 Oe for Fe_3O_4, SiO_2/Fe_3O_4, V_2O_5/Fe_3O_4, and $V_2O_5/SiO_2/Fe_3O_4$, respectively, accompanied by low remanent magnetization (Mr) values of 1.16, 1.47, 1.62, and 1.50 emu g^{-1}. These consistently low Hc and Mr values indicate superparamagnetic-like behavior at room temperature, rather than conventional ferromagnetism, as thermal fluctuations are sufficient to randomize the magnetic moments once the external magnetic field is removed.

Pure Fe_3O_4 exhibits the highest saturation magnetization (Ms) value of 82.4 emu g^{-1}. Successive surface modification leads to a gradual decrease in Ms to 75.4 emu g^{-1} for SiO_2/Fe_3O_4 and 61.3 emu g^{-1} for $V_2O_5/SiO_2/Fe_3O_4$. A more pronounced reduction to 22.6 emu g^{-1} is observed for V_2O_5/Fe_3O_4, indicating a stronger influence of V_2O_5 incorporation on the magnetic response.

The decrease in saturation magnetization observed for the composite samples is attributed primarily to magnetic dilution, arising from the incorporation of non–magnetic SiO_2 and V_2O_5 phases. These phases reduce the effective Fe_3O_4 mass fraction and weaken magnetic dipole–dipole interactions, consistent with previous reports [39–41]. In the case of V_2O_5/Fe_3O_4, the notably lower Ms value may also

be partially attributed to oxidation of Fe_3O_4 to hematite (α–Fe_2O_3) during thermal treatment, in agreement with the hematite reflections observed in the XRD patterns.

Despite the reduction in saturation magnetization, all composite catalysts retain low and comparable coercivity values, indicating that surface coating with SiO_2 and incorporation of V_2O_5 do not significantly alter the magnetic anisotropy or domain structure of the Fe_3O_4 core. This preservation of intrinsic magnetic characteristics ensures reliable magnetic separability.

Overall, the VSM results demonstrate that the $V_2O_5/SiO_2/Fe_3O_4$ catalyst maintains sufficient magnetic responsiveness for rapid recovery using an external magnetic field, while simultaneously providing a structurally stable and recyclable multifunctional platform for heterogeneous catalysis.

3.1.9 XPS analysis

X–ray photoelectron spectroscopy (XPS) was employed to analyze the surface chemical composition and oxidation states of the 20 wt% $V_2O_5/SiO_2/Fe_3O_4$ composite catalyst, which are directly related to its catalytic activity (Figure 9). The survey spectrum (Figure 9a) confirms the presence of V, Si, Fe, O, and C on the catalyst surface. The C 1s spectrum (Figure 9b) exhibits peaks at 284.4 and 285.0 eV, which are assigned to C–C/C–H and C–O functional groups, respectively. These signals originate from adventitious surface carbon and were used for charge correction during XPS analysis [42].

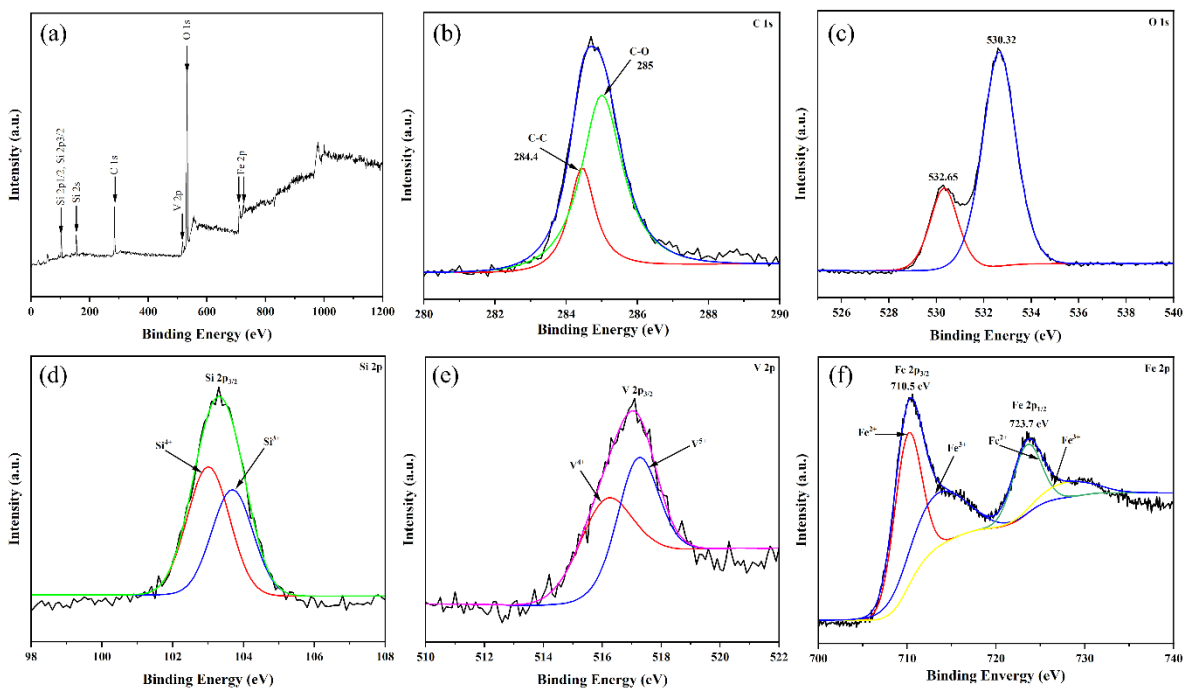

Figure 9: XPS spectra of the 20 wt% $V_2O_5/SiO_2/Fe_3O_4$ catalyst: (a) survey spectrum and high–resolution spectra of (b) C 1s, (c) O 1s, (d) Si 2p, (e) V 2p, and (f) Fe 2p.

The O 1s spectrum (Figure 9c) exhibits a main peak at 530.32 eV corresponding to lattice oxygen, along with a higher–binding–energy component at 532.65 eV attributed to adsorbed oxygen species [43]. The Si 2p spectrum (Figure 9d) displays two peaks at 103.0 eV and 103.8 eV, corresponding to Si^{3+} and Si^{4+} species, respectively. The dominant Si^{4+} peak at 103.8 eV confirms the presence of fully oxidized silicon, indicating a silica framework on the catalyst surface [44].

The V $2p_{3/2}$ region (Figure 9e) shows two contributions at 516.2 eV (V^{4+}) and 517.5 eV (V^{5+}), indicating that vanadium is predominantly present in the V^{5+} oxidation state, with a minor fraction of reduced vanadium likely arising from interfacial interactions with the Fe_3O_4 support. Although the

ketalization reaction is primarily acid-catalyzed rather than redox–driven, the coexistence of V^{5+}/V^{4+} species may influence surface acidity and catalyst stability rather than participating directly in redox activity. The Fe 2p spectrum (Figure 9f) exhibits Fe $2p_{3/2}$ peaks at 710.3 eV (Fe^{3+}) and 714.0 eV (satellite), together with Fe $2p_{1/2}$ peaks at 723.7 and 728.0 eV, confirming the coexistence of Fe^{2+} and Fe^{3+} species characteristic of magnetite (Fe_3O_4) [45].

Collectively, the XPS results confirm the successful formation of the ternary $V_2O_5/SiO_2/Fe_3O_4$ composite and verify the preservation of oxidized silica, mixed–valence iron oxide, and catalytically active vanadium species on the catalyst surface.

3.2 *Catalytic Activities*

3.2.1 Effect of reaction temperature

The influence of reaction temperature on glycerol ketalization with acetone was initially evaluated by comparing catalytic performance at room temperature and reflux conditions using the 15 wt% $V_2O_5/SiO_2/Fe_3O_4$ catalyst (Figure 10). A significant increase in both glycerol conversion and solketal selectivity was observed with increasing temperature.

At room temperature, the reaction achieved a glycerol conversion of 75.64%, with solketal as the dominant product (selectivity: 64.92%) and acetal as a secondary product (31.39%). Although noticeable catalytic activity was observed under these mild conditions, the overall reaction rate is primarily limited by mass transfer and transport phenomena, which are commonly encountered in reactions involving viscous polyols such as glycerol. At lower temperatures, glycerol exhibits high viscosity and reduced molecular diffusivity, which significantly restricts its mobility from the bulk liquid phase to the catalyst surface. As a consequence, the diffusion of glycerol to the active sites becomes the rate–limiting step, leading to incomplete utilization of the available catalytic sites. This diffusion constraint reduces effective reactant–catalyst contact and prevents the reaction system from operating under intrinsic kinetic control, thereby limiting both conversion and selectivity toward the desired solketal product.

The moderate conversion at room temperature can also be interpreted through collision theory. At reduced temperatures, glycerol and acetone molecules possess lower kinetic energy, resulting in fewer effective collisions capable of surpassing the activation energy barrier [46]. As a result, even in the presence of accessible catalytic sites, the number of productive molecular interactions remains limited.

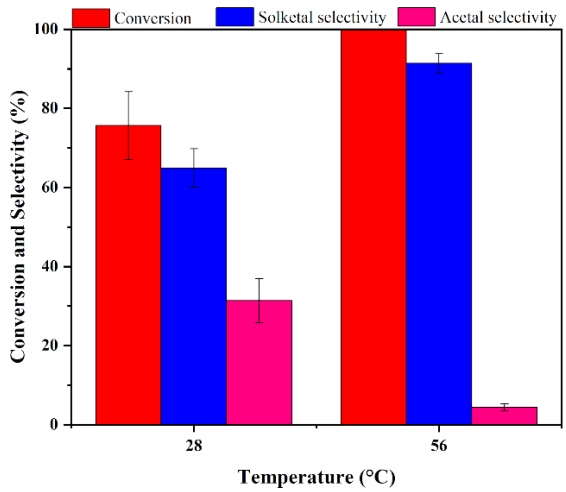

Figure 10: Effect of reaction temperature on glycerol ketalization over the 15 wt% $V_2O_5/SiO_2/Fe_3O_4$ catalyst. Reaction conditions: glycerol (1 mmol), acetone (20 mL), catalyst (50 mg), reaction time 4 h, at room temperature and reflux.

When the reaction temperature was increased to reflux, the catalytic performance improved markedly, reaching complete glycerol conversion (100%). Simultaneously, selectivity toward solketal rose to 91.38%, while acetal selectivity decreased significantly to 4.34%. This improvement can be attributed to several synergistic effects. First, elevated temperature lowers the viscosity of glycerol and improves its miscibility with acetone, thereby reducing external and internal mass–transfer limitations and allowing rapid transport of reactants to the catalyst surface. Second, higher thermal energy increases molecular collision frequency and energy, enabling a greater proportion of collisions to exceed the activation energy threshold and accelerating intrinsic reaction kinetics [13], [47].

Under optimized thermal conditions, the formation of the thermodynamically favored five–membered ring structure (solketal) becomes predominant, leading to enhanced selectivity. These results demonstrate that elevated temperature is essential not only for overcoming transport limitations but also for promoting efficient molecular interactions and directing reaction pathways toward the desired product.

Overall, the findings confirm that increasing reaction temperature effectively eliminates diffusion

barriers, enhances molecular reactivity, and drives the system into a kinetic–controlled regime, thereby enabling complete glycerol conversion and highly selective solketal formation.

3.2.2 *Effect of various catalysts*

The pronounced differences in glycerol ketalization performance clearly demonstrate the strong influence of catalyst composition on both conversion and product selectivity. As shown in Figure 11, the reaction conducted without any catalyst and in the presence of SiO_2 alone resulted in zero glycerol conversion, indicating that these materials are catalytically inactive for this transformation.

Fe_3O_4 exhibited limited catalytic activity, achieving only 8.19% glycerol conversion with extremely low selectivity toward solketal (0.70%). This suggests that although Fe_3O_4 may provide a small number of potentially active surface sites, they are insufficient to promote efficient ketalization. Similarly, the 10 wt% V_2O_5/Fe_3O_4 catalyst displayed minimal improvement, with only 3.87% conversion and 1.33% solketal yield. This result indicates that at low V_2O_5 loading, vanadium species are either too sparsely distributed or insufficiently exposed to effectively catalyze the reaction.

In contrast, pure V_2O_5 displayed markedly improved performance, achieving 39.85% glycerol conversion with a solketal yield of 26.02%. This result confirms that V_2O_5 serves as the primary active phase, most likely due to the presence of strong Lewis and Brønsted acidic sites that facilitate protonation of the carbonyl group and formation of the ketal intermediate. Nevertheless, incomplete conversion and moderate selectivity indicate that V_2O_5 alone suffers from limited accessibility of active sites, poor dispersion, and possible deactivation by water produced during the reaction.

The highest catalytic performance was achieved with the 15 wt% $V_2O_5/SiO_2/Fe_3O_4$ catalyst, which exhibited complete glycerol conversion and a solketal yield of 91.38%. This outstanding performance can be attributed to the synergistic combination of the highly active V_2O_5 phase with the large surface area of SiO_2 and the dispersion enhancement provided by the Fe_3O_4 magnetic support. The silica framework improves exposure of active sites, mitigates aggregation of vanadium species, and enhances reactant diffusion, while Fe_3O_4 facilitates catalyst recovery and improves structural stability. Together, these effects create a well–balanced catalytic environment that strongly favors solketal formation.

Overall, these results clearly demonstrate that catalytic efficiency depends not only on the presence of acidic sites but also on their accessibility, dispersion, and cooperative interactions with support materials. The $V_2O_5/SiO_2/Fe_3O_4$ composite, therefore, represents a highly effective and practical catalyst for glycerol valorization.

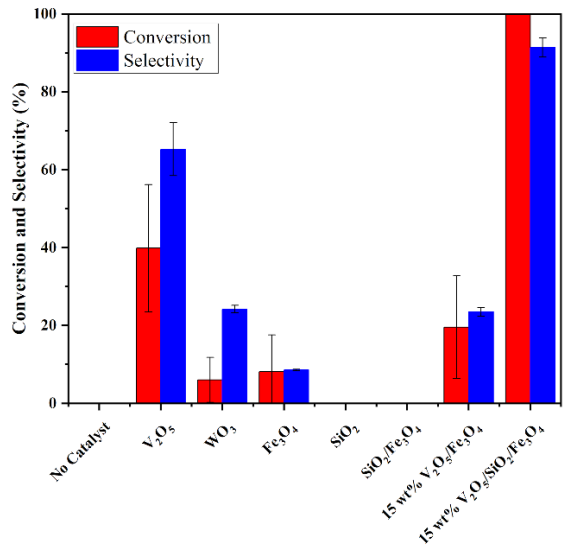

Figure 11: Effect of catalyst type on glycerol conversion and solketal selectivity. Reaction conditions: glycerol (1 mmol), acetone (20 mL), catalyst (50 mg), reaction time 4 h, under reflux.

3.2.3 *Effect of vanadium loading*

The influence of vanadium loading on catalytic performance was investigated by evaluating glycerol conversion, solketal yield, and selectivity at different vanadium contents (Figure 12). A strong correlation between vanadium loading and catalytic activity was observed.

As vanadium loading increased, glycerol conversion improved significantly, reaching complete conversion (100%) at both 20 wt% and 30 wt%. This indicates that increasing vanadium content enhances the density of acidic active sites responsible for promoting the ketalization reaction. A similar trend was observed for solketal yield, which increased with vanadium loading and reached a maximum value of 91.55% at 20 wt%.

However, a further increase in vanadium loading beyond the optimum led to a decline in solketal yield.

At 25 wt%, the solketal yield decreased to 76.44%, suggesting that excessive vanadium loading does not proportionally improve catalytic performance. This decrease may be attributed to partial blockage of active sites, reduced surface accessibility, or the formation of vanadium aggregates that limit effective dispersion on the support surface. In contrast, at lower vanadium contents (10 wt% and 15 wt%), both conversion and solketal yield were considerably lower, indicating insufficient active site density to drive the reaction efficiently.

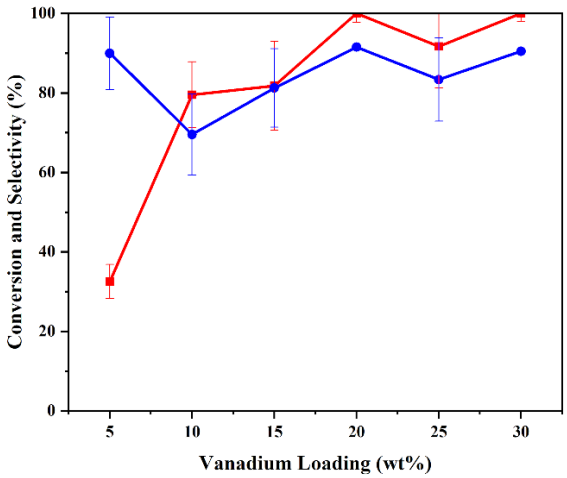

Figure 12: Effect of vanadium loading on glycerol conversion and solketal selectivity over $V_2O_5/SiO_2/Fe_3O_4$ catalysts. Reaction conditions: glycerol (1 mmol), acetone (20 mL), catalyst (50 mg), reaction time 4 h, under reflux.

Selectivity toward solketal was highest at a vanadium loading of 20 wt%, confirming this composition as the optimum condition that effectively balances high glycerol conversion with efficient formation of the desired product. At lower vanadium loadings, particularly at 10 wt%, a relatively high yield of by–products was observed (24.21%), indicating insufficient density of active acidic sites to selectively promote solketal formation. As the vanadium content increased, the yield of by–products decreased progressively, suggesting that higher vanadium loadings enhance the availability and strength of active sites, thereby suppressing undesired side reactions and favoring the selective formation of solketal.

Overall, these findings demonstrate that vanadium loading plays a critical role in governing both catalytic efficiency and product selectivity in the ketalization of glycerol. An optimal vanadium content of 20 wt% provides the most favorable balance between catalytic activity and selectivity, making it the most effective formulation for glycerol ketalization under the studied reaction conditions.

3.2.4 Effect of reaction time

The influence of reaction time on glycerol conversion and solketal selectivity was evaluated to determine the optimal duration for the ketalization reaction. As shown in Figure 13, both conversion and selectivity exhibit time–dependent behavior, reflecting the progressive development of catalytic activity and reaction equilibrium.

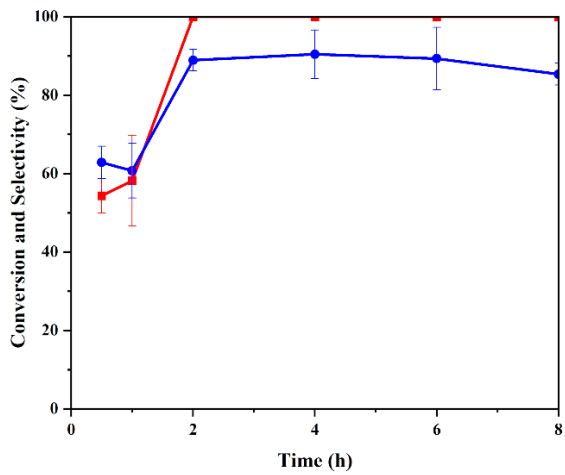

Figure 13: Effect of reaction time on glycerol conversion and solketal selectivity over the $V_2O_5/SiO_2/Fe_3O_4$ catalyst. Reaction conditions: glycerol (1 mmol), acetone (20 mL), catalyst (50 mg), under reflux.

At a reaction time of 0.5 h, glycerol conversion reached 54.33% with a solketal selectivity of 62.86%, indicating that the catalyst displays significant activity even at short reaction times. Extending the reaction to 1 h resulted in a moderate increase in conversion to 58.21%, although selectivity slightly decreased to 60.73%, suggesting the temporary formation of intermediate or side products.

Complete glycerol conversion (100%) was achieved after 2 h, accompanied by a notable improvement in solketal selectivity to 88.92%, indicating that sufficient residence time allows the reaction system to approach equilibrium while favoring solketal formation. At 4 h, conversion

remained quantitative and solketal selectivity increased further to a maximum of 90.43%, identifying this duration as the optimal reaction time for balancing conversion and selectivity.

Beyond 4 h, prolonged reaction time resulted in a gradual decline in selectivity, despite continued full conversion. At 6 h, a slight decrease in solketal selectivity was observed, while further extension to 8 h led to a more noticeable reduction to 85.35%. This decline can be attributed to secondary reactions such as hydrolysis, oligomerization, or solvent–induced transformation occurring under extended thermal exposure.

Overall, these results demonstrate that while glycerol conversion is rapidly achieved, prolonged reaction times are unfavorable for selectivity. An optimal reaction time of 4 h provides the best compromise between complete glycerol conversion and maximum solketal selectivity.

3.2.5 Effect of catalyst loading

The impact of catalyst loading on glycerol ketalization was investigated using catalyst amounts ranging from 10 to 50 mg, as shown in Figure 14.

At the lowest loading (10 mg), glycerol conversion was limited to 55.88% with a solketal selectivity of 89.38%, indicating insufficient availability of active sites to drive the reaction effectively. Increasing the catalyst loading to 20 mg significantly improved catalytic performance, resulting in a conversion of 74.77% and selectivity of 94.13%. This increase indicates improved contact between reactants and active sites, leading to enhanced reaction kinetics.

The optimal performance was observed at a catalyst loading of 40 mg, achieving a maximum glycerol conversion of 91.34% and outstanding solketal selectivity of 99.65%. This demonstrates that 40 mg provides the most favorable balance between active site availability and mass transfer under the investigated conditions.

Further increasing the catalyst loading to 50 mg led to a decline in performance, with conversion dropping to 85.98% and selectivity to 95.08%. This decrease may be attributed to particle agglomeration, increased slurry viscosity, or partial blockage of catalytic sites due to excessive solid content, which together hinder effective mass transfer and reduce catalyst utilization efficiency.

Overall, these results indicate that catalyst loading plays a crucial role in determining both reaction rate and product distribution. An optimal catalyst amount is required to maximize catalytic efficiency while avoiding transport limitations, and under these conditions, 40 mg represents the ideal loading for glycerol ketalization.

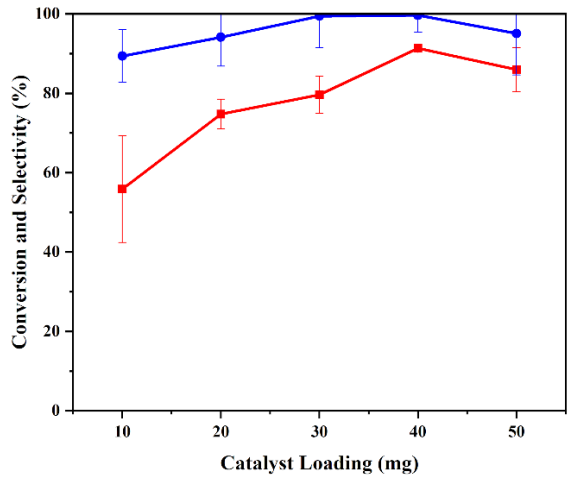

Figure 14: Effect of catalyst loading on glycerol conversion and solketal selectivity over the 20 wt% $V_2O_5/SiO_2/Fe_3O_4$ catalyst. Reaction conditions: glycerol (1 mmol), catalyst (10–50 mg), acetone (20 mL), reaction time 4 h, under reflux.

3.2.6 Recyclability

The recyclability of the $V_2O_5/SiO_2/Fe_3O_4$ catalyst was evaluated over three consecutive reaction cycles to assess its operational stability. After each cycle, the catalyst was separated using an external magnetic field, thoroughly washed with acetone under stirring to remove adsorbed species, and dried at 100 °C for 5 h before reuse.

The catalyst exhibited high initial activity and excellent selectivity toward solketal formation, with only minor variations observed during the first two reuse cycles. Although a gradual decrease in glycerol conversion was observed in the third cycle, solketal selectivity remained consistently high. This indicates that the nature and strength of the active sites responsible for ketal formation were largely preserved during repeated use.

To address catalyst loss during recycling, the recovered catalyst mass was weighed after each cycle. A gradual mass loss of approximately 7% per cycle was observed, mainly arising from handling, washing, and magnetic separation steps. Importantly, the recovered catalyst was reused without replenishment,

and catalytic performance in subsequent cycles was evaluated based on the actual recovered catalyst mass. Therefore, the observed decrease in conversion is attributed primarily to the reduced amount of catalyst available rather than intrinsic catalyst deactivation.

Overall, these results demonstrate that the $V_2O_5/SiO_2/Fe_3O_4$ catalyst maintains its structural integrity and catalytic functionality under repeated reaction conditions. The combination of stable solketal selectivity, preserved active sites, and efficient magnetic recovery confirms the good recyclability and operational durability of the composite catalyst, highlighting its potential as a sustainable heterogeneous catalytic system. The recyclability performance is presented in Figure 15.

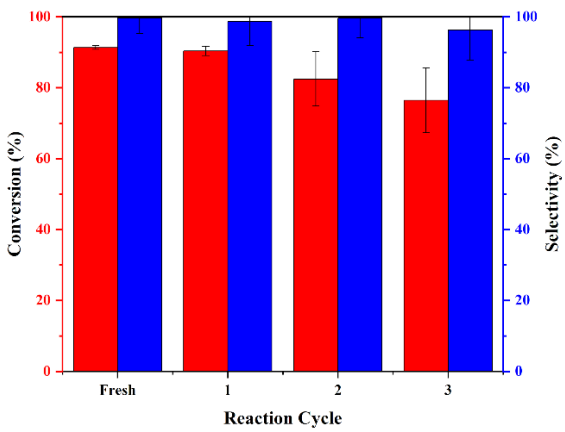

Figure 15: Recyclability of the 20 wt% $V_2O_5/SiO_2/Fe_3O_4$ catalyst for glycerol ketalization. Reaction conditions: glycerol (1 mmol), catalyst (40 mg), acetone (20 mL), reaction time 4 h, under reflux.

4 Conclusions

The sustainable conversion of glycerol into value-added chemicals is crucial for improving both the economic viability and environmental sustainability of biodiesel production. In this study, we demonstrate that rational catalyst architecture, rather than active phase selection alone, is a key factor in achieving high catalytic performance and recyclability in glycerol ketalization.

The central contribution of this work is the identification of a SiO_2 interlayer–mediated design principle for magnetically recoverable catalysts. The introduction of a SiO_2 interlayer between the Fe_3O_4 magnetic core and the V_2O_5 active phase acts as a physical and chemical mediator, preventing direct contact between Fe_3O_4 and V_2O_5. This interfacial separation suppresses particle aggregation, stabilizes vanadium oxidation states, and preserves the magnetic integrity of the catalyst.

Comprehensive structural and surface characterization (XRD, BET, SEM, HR–TEM, VSM, XRF, FTIR, and XPS) confirms that this architecture yields a synergistic catalyst system in which acidity, dispersion, and magnetic recoverability are simultaneously maintained. As a result of this design, the 20 wt% $V_2O_5/SiO_2/Fe_3O_4$ catalyst exhibits high glycerol conversion and excellent selectivity toward solketal under optimized conditions. The observed catalytic performance arises primarily from the Lewis acidic nature of V_2O_5, combined with SiO_2–enabled dispersion and stabilization of the active sites, which enhances reactant accessibility and reaction efficiency.

Importantly, the Fe_3O_4 core enables rapid magnetic separation, while the SiO_2 interlayer contributes to structural stability during repeated use. This synergistic integration allows the catalyst to retain high activity over multiple reaction cycles with minimal performance loss, effectively addressing common challenges in glycerol ketalization catalysts related to limited durability and difficult recovery.

Overall, this work advances the field beyond existing glycerol ketalization catalysts by establishing a clear and transferable interlayer–mediated design strategy that integrates catalytic activity, stability, and magnetic recyclability within a single material. The $V_2O_5/SiO_2/Fe_3O_4$ system thus provides both a practical solution for glycerol valorization and a general framework for the rational design of multifunctional heterogeneous catalysts for sustainable chemical processes.

Acknowledgments

Ado Ibrahim Yargaya gratefully acknowledges financial support from the KMUTT international Scholarship Program (KISP). This research project is supported by King Mongkut's University of Technology Thonburi (KMUTT), Thailand Science Research and Innovation (TSRI), and National Science, Research and Innovation Fund (NSRF) Fiscal year 2025 Grant number FRB680074/0164.

Author Contributions

A.I.Y.: writing an original draft, investigation, data curation, validation; V.L.: data curation. P.T. and M.S.: writing-reviewing and editing; K.C.: writing-

reviewing and editing, validation, supervision, resources, funding acquisition, conceptualization. All authors have read and agreed to the published this version of the manuscript.

Conflicts of Interest

The authors declare no conflict of interest.

Declaration of generative AI and AI-assisted technologies in the writing process

The authors utilized the ChatGPT tool to enhance the language and readability of the manuscript.

Appendix A. Supplementary data

Supplementary data to this article can be found online here.

References

[1] T. Dhanakoses *et al.,* "Engineering surface hydrophobicity in zeolites for efficient biphasic glycerol–acetone acetalization," *Energy & Fuels*, vol. 39, no. 41, pp. 19747–19759, 2025, doi: 10.1021/acs.energyfuels.5c03988.

[2] S. Maurya and Y. C. Sharma, "A facile approach for the synthesis of solketal, a fuel additive, from biowaste glycerol using transition metal-based solid acid catalysts," *RSC Advances*, vol. 14, no. 53, pp. 39511–39522, 2024, doi: 10.1039/d4ra05455e.

[3] R. Li, H. Li, P. Wang, Z. Wei, Z. Yin, and Z. Wang, "Ketalization of glycerol with acetone to solketal over a phenolic resin-based solid acid," *Industrial Crops and Products*, vol. 221, p. 119345, 2024, doi: 10.1016/j.indcrop.2024.119345.

[4] I. Corrêa, R. P. V. Faria, and A. E. Rodrigues, "Continuous valorization of glycerol into solketal: recent advances on catalysts, processes, and industrial perspectives," *Sustainable Chemistry*, vol. 2, no. 2, pp. 286–324, 2021, doi: 10.3390/suschem2020017.

[5] J. A. Melero, G. Vicente, G. Morales, M. Paniagua, and J. Bustamante, "Oxygenated compounds derived from glycerol for biodiesel formulation: Influence on EN 14214 quality parameters," *Fuel*, vol. 89, no. 8, pp. 2011–2018, 2010, doi: 10.1016/j.fuel.2010.03.042.

[6] P. H. R. Silva, V. L. C. Gonçalves, and C. J. A. Mota, "Glycerol acetals as anti-freezing additives for biodiesel," *Bioresource Technology*, vol. 101, no. 15, pp. 6225–6229, 2010, doi: 10.1016/j.biortech.2010.02.101.

[7] F. M. Perez, C. Legarto, M. B. Lombardi, G. F. Santori, F. Pompeo, and N. N. Nichio, "Activated bentonite nanocomposite for the synthesis of solketal from glycerol in the liquid phase," *Catalysts*, vol. 12, no. 6, p. 673, 2022, doi: 10.3390/catal12060673.

[8] C. J. Mota, C. X. da Silva, N. Rosenbach Jr, J. Costa, and F. da Silva, "Glycerin derivatives as fuel additives: the addition of glycerol/acetone ketal (solketal) in gasolines," *Energy & Fuels*, vol. 24, no. 4, pp. 2733–2736, 2010, doi: 10.1021/ef9015735.

[9] L. P. Ozorio, R. Pianzolli, M. B. S. Mota, and C. J. Mota, "Reactivity of glycerol/acetone ketal (solketal) and glycerol/formaldehyde acetals toward acid-catalyzed hydrolysis," *Journal of the Brazilian Chemical Society*, vol. 23, pp. 931–937, 2012, doi: 10.1590/s0103-50532012000500019.

[10] M. R. Nanda, Y. Zhang, Z. Yuan, W. Qin, H. S. Ghaziaskar, and C. C. Xu, "Catalytic conversion of glycerol for sustainable production of solketal as a fuel additive: A review," *Renewable and Sustainable Energy Reviews*, vol. 56, pp. 1022–1031, 2016, doi: 10.1016/j.rser.2015.12.008.

[11] I. Zahid et al., "Production of fuel additive solketal via catalytic conversion of biodiesel-derived glycerol," *Industrial & Engineering Chemistry Research*, vol. 59, no. 48, pp. 20961–20978, 2020, doi: 10.1021/acs.iecr.0c04123.

[12] J. Esteban, A. J. Vorholt, A. Behr, M. Ladero, and F. Garcia-Ochoa, "Liquid–liquid equilibria for the system acetone+ solketal+ glycerol at (303.2, 313.2, and 323.2) K," *Journal of Chemical and Engineering Data*, vol. 59, no. 9, pp. 2850–2855, 2014, doi: 10.1021/je500469a.

[13] J. A. Vannucci, N. N. Nichio, and F. Pompeo, "Solketal synthesis from ketalization of glycerol with acetone: a kinetic study over a sulfated zirconia catalyst," *Catalysis Today*, vol. 372, pp. 238–245, 2021, doi: 10.1016/j.cattod.2020.10.005.

[14] I. B. Laskar, K. Rajkumari, R. Gupta, and S. L. Rokhum, "Acid-functionalized mesoporous polymer-catalyzed acetalization of glycerol to solketal, a potential fuel additive under solvent-free conditions," *Energy & Fuels*, vol. 32, no. 12, pp. 12567–12576, 2018, doi: 10.1021/acs.energyfuels.8b02948.

[15] S. Ao, S. P. Gouda, L. Saikia, B. Gurunathan, and S. L. Rokhum, "Biochar carbon nanodots for

catalytic acetalization of biodiesel by-product crude glycerol to solketal: process optimization by RSM and life cycle cost analysis," *Scientific Reports*, vol. 14, no. 1, p. 20140, 2024, doi: 10.1038/s41598-024-69553-7.

[16] F. C. Ballotin, M. J. da Silva, A. P. de Carvalho Teixeira, and R. M. Lago, "Amphiphilic acid carbon catalysts produced by bio-oil sulfonation for solvent-free glycerol ketalization," *Fuel*, vol. 274, p. 117799, 2020, doi: 10.1016/j.fuel.2020.117799.

[17] A. d. M. Barboza et al., "Effect of iron and molybdenum on silica-based mesoporous catalysts for glycerol conversion to solketal," *Molecular Catalysis*, vol. 584, p. 115302, 2025, doi: 10.1016/j.mcat.2025.115302.

[18] A. Vivian et al., "The high activity of mesoporous Ga-SiO_2 catalysts in the upgrading of glycerol to solketal explained by in-depth characterization," *Journal of Catalysis*, vol. 400, pp. 83–92, 2021, doi: 10.1016/j.jcat.2021.05.017.

[19] N. Chansorn, S. Amnuaypanich, S. Soontaranon, S. Rugmai, and S. Amnuaypanich, "Increasing solketal production from the solventless ketalization of glycerol catalyzed by nanodispersed phosphotungstic acid in poly(N-methyl-4-vinylpyridinium) grafted on silica nanoparticles," *Journal of Industrial and Engineering Chemistry*, vol. 112, pp. 233–243, 2022, doi: 10.1016/j.jiec.2022.05.017.

[20] X. Meng, X. Xin, T. Zhang, Y. Yu, and Y. Cheng, "Preparation of millimeter-sized spherical SiO_2–Al_2O_3 with various acid catalysts for the acetalization of glycerol with acetone," *Journal of Porous Materials*, vol. 31, no. 3, pp. 1015–1027, 2024, doi: 10.1007/s10934-024-01558-z.

[21] L. Aguado-Deblas, R. Estevez, M. Russo, V. La Parola, F. M. Bautista, and M. L. Testa, "Sustainable microwave-assisted solketal synthesis over sulfonic silica-based catalysts," *Journal of Environmental Chemical Engineering*, vol. 10, no. 6, p. 108628, 2022, doi: 10.1016/j.jece.2022.108628.

[22] A. A. Q. Ali and Z. N. Siddiqui, "Heteropoly ionic liquid functionalized MOF-Fe: Synthesis, characterization, and catalytic application in selective acetalization of glycerol to solketal as a fuel additive at room temperature, solvent-free conditions," *Precision Chemistry*, vol. 1, no. 8, pp. 485–496, 2023, doi: 10.1021/prechem.3c00017.

[23] K. Rajkumari et al., "A reusable magnetic nanocatalyst for bio-fuel additives: The ultrasound-assisted synthesis of solketal," *Sustainable Energy & Fuels*, vol. 5, no. 8, pp. 2362–2372, 2021, doi: 10.1039/d0se01900c.

[24] R. K. Singh, V. Gosu, and V. Subbaramaiah, "Synthesis of oxygenated fuel additive solketal through catalytic acetalization of glycerol with acetone using HPMo/AlTUD-1," *Biomass and Bioenergy*, vol. 193, p. 107553, 2025, doi: 10.1016/j.biombioe.2024.107553.

[25] J. Kowalska-Kuś et al., "Synthesis of solketal catalyzed by acid-modified pyrolytic carbon black from waste tires," *Molecules*, vol. 29, no. 17, p. 4102, 2024, doi: 10.3390/molecules29174102.

[26] W. Wang and H. Gong, "Efficiently catalytic glycerol to solketal through acetalization over sulfated UiO-66," *Polyhedron*, vol. 269, p. 117407, 2025, doi: 10.1016/j.poly.2025.117407.

[27] Y. Ce, W. Jiajia, and H. Yanglong, "Fe_3O_4 nanostructures: Synthesis, growth mechanism, properties and applications," *Chemical Communications*, vol. 47, pp. 5130–5141, 2011, doi: 10.1039/c0cc05862a.

[28] S. Bosoy, S. Intachai, P. Sumanatrakul, P. Kongsune, S. Loiha, and N. Khaorapapong, "Novel magnetic composite: NiFe-layered double oxide/ferric oxyhydroxide/activated carbon for optimizing biodiesel production from used cooking oil," *Biomass and Bioenergy*, vol. 183, p. 107096, 2024, doi: 10.1016/j.biombioe.2024.107096.

[29] S. Intachai, P. Sumanatrakul, C. Chaiburi, A. Pewhom, P. Nuengmatcha, and N. Khaorapapong, "Green and facile assembly of LDO, AC, FeOOH and Fe_3O_4 as multifunctional composite catalyst for efficient biodiesel production and dye degradation," *Fuel*, vol. 371, p. 132041, 2024, doi: 10.1016/j.fuel.2024.132041.

[30] K. Sangthong, P. Sumanatrakul, N. Khaorapapong, and S. Intachai, "Highly enhanced adsorption and photodegradation of various dyes in wastewater: Novel multifunctional composites of CuAl-layered double oxide, activated carbon and magnetite," *Diamond and Related Materials*, vol. 158, p. 112618, 2025, doi: 10.1016/j.diamond.2025.112618.

[31] V. Mounasamy, G. Srividhya, and N. Ponpandian, "Well-defined 2D transition

vanadium pentoxide (V_2O_5) flat nanorods with large-scale synthesis feasibility as an electrocatalyst for the oxygen evolution reaction (OER)," *Energy Advances*, vol. 2, no. 6, pp. 784–788, 2023, doi: 10.1039/d3ya00100h.

[32] I. N. Reddy, B. Akkinepally, V. Manjunath, G. Neelima, M. V. Reddy, and J. Shim, "SnO_2 quantum dots distributed along V_2O_5 nanobelts for utilization as a high-capacity storage hybrid material in Li-ion batteries," *Molecules*, vol. 26, no. 23, p. 7262, 2021, doi: 10.3390/molecules26237262.

[33] A. Diego-Lopez, O. Cabezuelo, A. Vidal-Moya, M. L. Marin, and F. Bosca, "Synthesis and mechanistic insights of SiO_2@WO_3@Fe_3O_4 as a novel supported photocatalyst for wastewater remediation under visible light," *Applied Materials Today*, vol. 33, p. 101879, 2023, doi: 10.1016/j.apmt.2023.101879.

[34] M. A. Ghasemzadeh, "Preparation and application of Fe_3O_4@SiO_2@OSO_3H nanocomposite as a green catalyst for the synthesis of octahydroquinazolinones," *Journal of Applied Chemical Research*, vol. 13, no. 1, pp. 8–23, 2019.

[35] Y. Saputra, A. I. Yargaya, A. M. Sani, A. Y. Abdurrahman, V. Luckanawat, and K. Chaiseeda, "Magnetically recoverable WO_3/Fe_3O_4 catalyst for the selective oxidation of styrene to benzaldehyde," *ACS Omega*, vol. 10, no. 34, pp. 38814–38825, 2025, doi: 10.1021/acsomega.5c04095.

[36] S. L. Khillare, M. K. Lande, N. S. Shinde, and B. R. Arbad, "Synthesis, characterization and catalytic application of V_2O_5/Fe_3O_4 as heterogeneous catalyst for the synthesis of quinoline-4-carboxylic acid derivatives " *Der Pharma Chemica*, vol. 9, no. 6, pp. 30–36, 2017.

[37] K. S. Sing, "Reporting physisorption data for gas/solid systems with special reference to the determination of surface area and porosity (Recommendations 1984)," *Pure and Applied Chemistry*, vol. 57, no. 4, pp. 603–619, 1985, doi: 10.1351/pac198557040603.

[38] Aashima et al., "Magnetically retrievable Ce-doped Fe_3O_4 nanoparticles as scaffolds for the removal of azo dyes," *RSC Advances*, vol. 9, no. 40, pp. 23129–23141, 2019, doi: 10.1039/c9ra03252e.

[39] L. You et al., "Facile synthesis of Fe_3O_4@COF covalent organic frameworks for the adsorption of bisphenols from aqueous solution," *Journal of Molecular Liquids*, vol. 320, p. 114456, 2020, doi: 10.1016/j.molliq.2020.114456.

[40] N. Rostami, M. G. Dekamin, E. Valiey, and H. FaniMoghadam, "l-Asparagine–EDTA–amide silica-coated MNPs: A highly efficient and nano-ordered multifunctional core–shell organocatalyst for green synthesis of 3, 4-dihydropyrimidin-2 (1 H)-one compounds," *RSC Advances*, vol. 12, no. 34, pp. 21742–21759, 2022, doi: 10.1039/d2ra02935a.

[41] N. Niedbut et al., "Multifunctional magnetic composite: MgAl-layered double hydroxide, activated carbon and magnetite on removing both different charged-dyes," *Chemical Engineering Science*, vol. 287, p. 119783, 2024, doi: 10.1016/j.ces.2024.119783.

[42] L. H. Grey, H.-Y. Nie, and M. C. Biesinger, "Defining the nature of adventitious carbon and improving its merit as a charge correction reference for XPS," *Applied Surface Science*, vol. 653, p. 159319, 2024, doi: 10.1016/j.apsusc.2024.159319.

[43] A. F. Zedan, S. Moussa, and M. S. El-Shall, "Facile microwave synthesis of various-shaped magnetite/ reduced graphene oxide heterostructures and their magnetization properties," *Scientific Reports*, vol. 14, no. 1, p. 22008, 2024, doi: 10.1038/s41598-024-71537-6.

[44] M. Yoshimizu et al., "Photocatalytic hydrogen evolution over β-Iron silicide under infrared light irradiation," *Chemical Communications*, vol. 51, pp. 2818–2820, 2015, doi: 10.1039/c4cc08093a.

[45] S. J. Yin, X. Wang, H. Jiang, M. Lu, and F. Q. Yang, "Preparation of yolk-shell structure NH(2)-MIL-125 magnetic nanoparticles for the selective extraction of nucleotides," *Mikrochimica Acta*, vol. 188, no. 12, p. 419, 2021, doi: 10.1007/s00604-021-05071-x.

[46] P. Atkins, J. De Paula, and R. Friedman, *Physical Chemistry: Quanta, Matter, and Change*. 2nd ed., Oxford, UK: Oxford University Press, 2014.

[47] M. N. Moreira, R. P. V. Faria, A. M. Ribeiro, and A. E. Rodrigues, "Solketal production from glycerol ketalization with acetone: Catalyst selection and thermodynamic and kinetic reaction study," *Industrial & Engineering Chemistry Research*, vol. 58, no. 38, pp. 17746–17759, 2019, doi: 10.1021/acs.iecr.9b03725.